SCIENTIFIC REPORTS

OPEN

CONFERENCE PROCEEDINGS

ACSMS2014

SUBJECT AREAS:
BATTERIES
ELECTRONIC DEVICES

Received
21 August 2014

Accepted
20 October 2014

Published
13 November 2014

Correspondence and requests for materials should be addressed to J.W. (jiazhao@uow.edu.au)

In-situ One-step Hydrothermal Synthesis of a Lead Germanate-Graphene Composite as a Novel Anode Material for Lithium-Ion Batteries

Jun Wang[1], Chuan-qi Feng[2], Zi-qi Sun[1], Shu-lei Chou[1], Hua-Kun Liu[1] & Jia-zhao Wang[1]

[1]Institute for Superconducting and Electronic Materials, University of Wollongong, Wollongong, NSW 2522, Australia, [2]Hubei Collaborative Innovation Center for Advanced Organic Chemical Materials, Hubei University, Wuhan 430062, P.R. China.

Lead germanate-graphene nanosheets ($PbGeO_3$-GNS) composites have been prepared by an efficient one-step, in-situ hydrothermal method and were used as anode materials for Li-ion batteries (LIBs). The $PbGeO_3$ nanowires, around 100–200 nm in diameter, are highly encapsulated in a graphene matrix. The lithiation and de-lithiation reaction mechanisms of the $PbGeO_3$ anode during the charge-discharge processes have been investigated by X-ray diffraction and electrochemical characterization. Compared with pure $PbGeO_3$ anode, dramatic improvements in the electrochemical performance of the composite anodes have been obtained. In the voltage window of 0.01–1.50 V, the composite anode with 20 wt.% GNS delivers a discharge capacity of 607 mAh g^{-1} at 100 mA g^{-1} after 50 cycles. Even at a high current density of 1600 mA g^{-1}, a capacity of 406 mAh g^{-1} can be achieved. Therefore, the $PbGeO_3$-GNS composite can be considered as a potential anode material for lithium ion batteries.

Lithium-ion batteries (LIBs) have been mainly used for portable electronics, but their use is now being extended to large-scale energy storage, such as in power tools and vehicle electrification[1–3]. In order to further improve the performance of LIBs, high energy density materials are desired, since graphite, the commercial anode, possesses low practical capacity. Ge has been intensively researched as an alternative anode material, owing to its high theoretical capacity (1600 mAh g^{-1}), low working potential, and high lithium ion diffusivity (400 times higher than that of the well-studied Si)[4,5]. This makes Ge a promising anode material for both high energy and high power applications. Pure Ge anode suffers from rapid capacity loss, however, accompanied by a huge irreversible capacity. The main reason is that the dramatic Ge volume changes and agglomeration during Li insertion/extraction processes lead to the pulverization and exfoliation of the active material, electrically isolating the particles from the current collector and degrading their cycling performance[6,7].

Tremendous efforts have been made to address this issue, including reducing the anode material to the nanoscale, construction of porous architectures, and amorphization of the anode material[8–11]. Recently, it has been proposed that preparing metal germanate nanowires or nanobelts could be a strategy to mitigate these problems[12–14]. The metal oxide matrix could provide an elastic buffer to accommodate the volume changes and prevent the agglomerations of nanosized Ge particles formed *in-situ* in the matrix after the initial discharge process, which could be helpful for improving the electrochemical performance of this material. Pb is a highly abundant element around the world, and its compounds exhibit good electrochemical performance as anode for LIBs[15,16], making $PbGeO_3$ an anode candidate to satisfy the growing demand for various energy-storage technologies. Since $PbGeO_3$ is actually an alkaline earth metal oxide, it is low in electrical conductivity, and its electrochemical performance is limited. $PbGeO_3$/PPy composites were reported to be prepared via a hydrothermal polymerization-coating method[17]. This technique is quite complicated and time-consuming, however, and the cycling stability and rate capability of the composites need to be improved. Therefore, it is still necessary to explore simple synthesis methods and an effective matrix for the formation of $PbGeO_3$ nanocomposite anode materials.

Graphene nanosheets (GNS), as two-dimensional macromolecular sheets of carbon atoms with a strongly bonded carbon network, have aroused explosive interest for energy-storage applications because they feature superior electrical conductivity, large theoretical specific surface area, and chemical tolerance, as well

as remarkable structural flexibility[18–20]. In the light of its fascinating advantages, it has been suggested that GNS could be an ideal substrate for the growth of functional nanomaterials for lithium storage. The hydrothermal method for preparing oxides and their composites with GNS is widely utilized because it allows control of the chemical composition, particle shape, and crystallite size in a simple and efficient way[21–24]. The *in-situ* one-step hydrothermal method can produce an *in-situ* coating of $PbGeO_3$ nanowires on wrinkled GNS and also simplify the synthesis method to reduce the cost and energy consumption.

Herein, a facile one-step hydrothermal method is employed to synthesize $PbGeO_3$-GNS composite as a novel anode material for LIBs. The metal oxides formed *in situ* after the initial discharge could help to alleviate the volume expansions during the lithium ion uptake/release. Moreover, the reversible reaction between Ge and Li_2O is presumed to improve the Li storage performance. Furthermore, the combination with the GNS enables fast electron migration for the Li-ion uptake/release in $PbGeO_3$, contributing to enhanced Li storage kinetics. In addition, embedding $PbGeO_3$ nanowires in the graphene (GN) matrix could also maintain the structural integrity of the composite anode by preventing large volume changes and particle agglomerations during cycling. Consequently, the composite anode exhibits superior electrochemical properties in terms of specific capacity, cycling stability, and rate capability compared to the pure $PbGeO_3$ anode.

Results

X-ray diffraction (XRD) patterns and FT-IR spectra for the pure $PbGeO_3$ and the $PbGeO_3$-GNS composites are presented in Fig. 1(a, b). The XRD patterns of the composites show that all the diffraction peaks can be well assigned to the hexagonal phase with lattice constants $a = 1.57$ nm and $c = 0.724$ nm (JCPDS 38-1035). The strong and clear peaks indicate the high crystallinity of the $PbGeO_3$ in the composites. Further information on the pure $PbGeO_3$, the $PbGeO_3$-GNS composites, and the GNS was provided by the associated Fourier transform infrared (FT-IR) spectroscopy. In the spectrum of the composites, the vibrations (transmittance peaks) located at 3452 cm^{-1} are related to the O-H stretching mode of intercalated water, and the vibrations (transmittance peaks) at around 1627 cm^{-1} can be ascribed to the C skeletal vibrations[25,26]. In the range of 400–1000 cm^{-1}, the vibrations (absorbance peak) are attributed to the characteristic mode of $PbGeO_3$, and the vibrations at around 841 and 419 cm^{-1} correspond to Ge-O and Pb-O bonds, respectively[17]. It should be noted that the transmittance peaks centred at around 1009 cm^{-1} appear in all the composites, but they cannot be traced in the $PbGeO_3$ and GNS. This is because they are associated with the stretching vibration of C-O, which cannot be reduced due to its interaction with the growth sites of $PbGeO_3$[27,28], indicating that $PbGeO_3$ is successfully anchored on the GNS by chemical bonds in the composites via the method mentioned above.

The weight percentages of the GNS in the $PbGeO_3$-GNS composites were obtained by means of thermogravimetric analysis (TGA), as shown in Fig. 1(c). The TGA was carried out from 25 to 900°C, with a heating rate of 10°C min^{-1} in air. Owing to the thermal stability of $PbGeO_3$, the pure $PbGeO_3$ remains stable, while the GNS was all burned out during the heating process. Therefore, the weight loss mainly results from the decomposition of the GNS, and the weight percent of the residue after 900°C is that of $PbGeO_3$ in the

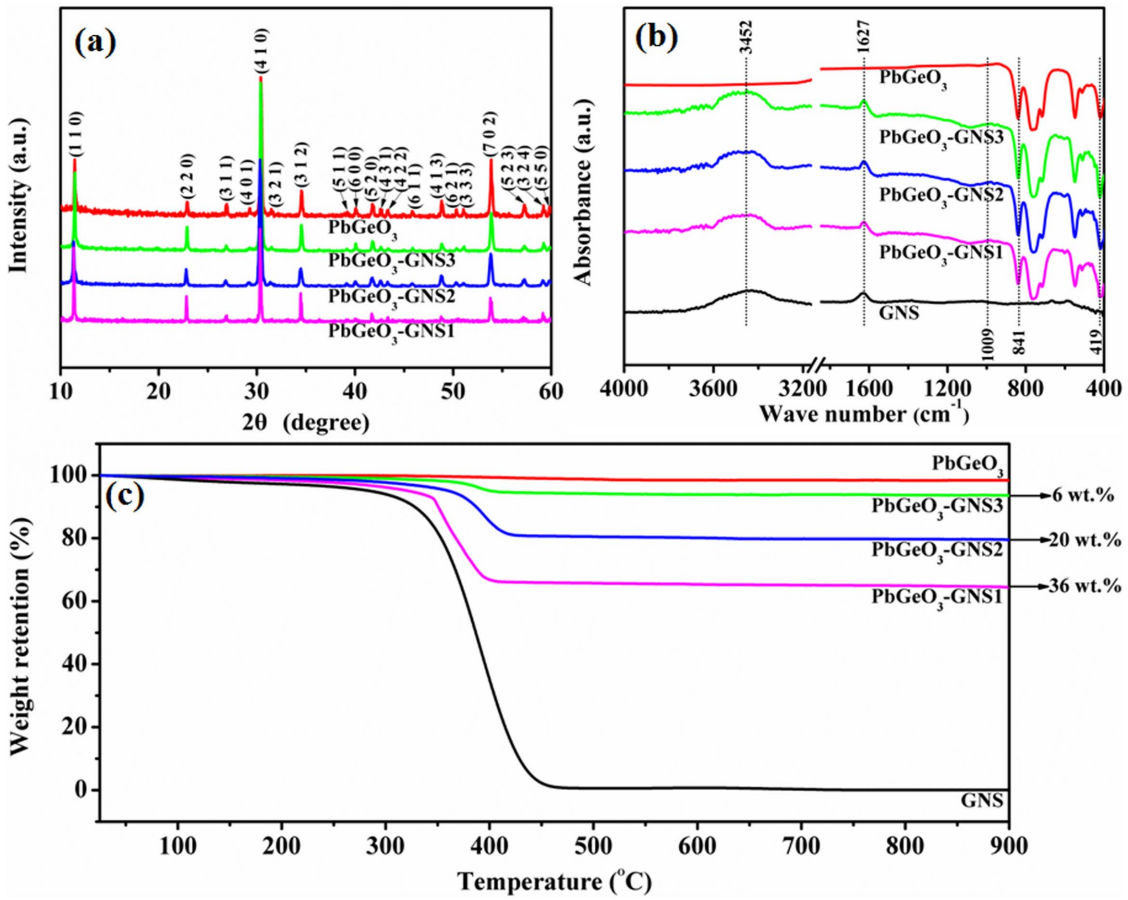

Figure 1 | (a) XRD patterns of the pure $PbGeO_3$ and the $PbGeO_3$-GNS composites; (b) FT-IR spectra of the pure $PbGeO_3$, the $PbGeO_3$-GNS composites, and the GNS; and (c) TGA curves of the pure $PbGeO_3$, the $PbGeO_3$-GNS (36, 20, and 6 wt.% of GNS) composites, and the GNS.

composite. Therefore, the GNS contents of the samples denoted as $PbGeO_3$-GNS1, $PbGeO_3$-GNS2, and $PbGeO_3$-GNS3 can be estimated to be approximately 36, 20, and 6 wt.%, respectively.

To investigate the morphology of the materials obtained, field emission scanning electron microscopy (FE-SEM) was performed on the pure $PbGeO_3$, the $PbGeO_3$-GNS2(20 wt.%) composite, and the GNS. By comparing with pure GNS and the $PbGeO_3$ [Fig. 2(a, b)], it can be seen clearly in Fig. 2(c) that the $PbGeO_3$ nanowires with a diameter of about 100 to 200 nm and the GNS form a sandwich-like structure, in which the GNS restack and the $PbGeO_3$ nanowires are homogeneously distributed on or between the GNS. Fig. 2(d) shows the associated energy-dispersive X-ray spectroscopy (EDS) of the $PbGeO_3$-GNS2 composite. Only the elements Pb, Ge, O and C were detected in the composite, which further proves that there are no other impurities in the sample. The transmission electron microscope (TEM) images in Fig. 2(e) confirmed the FE-SEM results and showed that the $PbGeO_3$ nanowires were uniformly dispersed in the GNS to form the composite. The typical high-resolution TEM image in Fig. 2(f) demonstrates that the $PbGeO_3$ nanowire was coated on the GNS with lattice spacing of 0.350 nm. The indexed diffraction spots in the fast Fourier transform (FFT) pattern of the $PbGeO_3$ selected area can be indexed to the (1 1 0), (2 0 1), and (1 $\bar{1}$ 1) planes of the hexagonal phase, respectively, and it can be seen that the preferential growth of the $PbGeO_3$ is along the [1 $\bar{1}$ 1] direction. There is also evidence that the $PbGeO_3$ lattice stripes are separated by 0.779 and 0.639 nm, corresponding to the (1 1 0) and (1 $\bar{1}$ 1) planes, respectively.

Fig. 3(a, b) shows cyclic voltammograms (CVs) of the $PbGeO_3$-GNS2(20 wt.%) anode and the pure $PbGeO_3$ anode. The $PbGeO_3$-GNS2 anode displays similar peak voltages to those of the pure $PbGeO_3$ anode during the first 5 cycles, where it is presumed that same charge and discharge reactions take place in the two anode materials. It can be seen, however, that the current density of the composite anode is much higher than that of the $PbGeO_3$ anode, and the CV curve of the $PbGeO_3$-GNS2 anode also exhibits better overlapping. That is because the $PbGeO_3$-GNS2 anode offers better kinetic properties, resulting from the GN wrapping, which greatly improves the electronic interparticle connections and prevents agglomeration during cycling[26,29].

Because the $PbGeO_3$ nanowires in the $PbGeO_3$ anode and $PbGeO_3$-GNS anodes are likely to be subject to the same Li storage mechanism, ex-situ XRD data on the $PbGeO_3$ anode were collected to identify it in detail, as shown in Fig. 3(c). Based on these results and the discharge–charge mechanisms of metal germanate, Pb and, Ge[6,12–14,30–36], the lithium ion intercalation and de-intercalation reactions of $PbGeO_3$ anode are proposed as the following reaction equations (1)–(4):

$$PbGeO_3 + 6Li^+ + 6e^- \rightarrow Pb + Ge + 3Li_2O \quad (1)$$

$$Pb + xLi^+ + xe^- \rightarrow Li_xPb \ (0 < x \leq 4.4) \quad (2)$$

$$Ge + yLi^+ + ye^- \rightarrow Li_yGe \ (0 < y \leq 4.4) \quad (3)$$

$$Ge + 2Li_2O \rightarrow GeO_2 + 4Li^+ + 4e^- \quad (4)$$

Remarkably, the first CV sweep is substantially different from the subsequent ones. Within the initial cathodic sweep, the broad peak between 1.4 and 1.0 V is related to the decomposition of $PbGeO_3$ into Pb, Ge, and Li_2O, accompanied by the formation of a solid electrolyte interphase (SEI) layer as well[13,23]. During the following scans, the broad decomposition peak disappears, and other evident peaks can be traced to processes that are activated after the 1st cycle. Specifically, three anodic peaks are associated with the de-alloying reactions of Li-Ge at 0.47 V[6] and Li-Pb at 0.47, 0.56, and 0.68 V[31], respectively. Partial oxidation of Ge by the Li_2O amorphous matrix to GeO_2 occurs from 1.0 to 1.3 V, and GeO_2 is then reversibly converted to Ge within the voltage range from 0.8 to 0.6 V in the anodic sweep[32,33]. It is well known, however, that Pb is relatively stable and cannot undergo a partially reversible reaction with Li_2O[34,35]. The alloying reactions of Li-Ge and Li-Pb occur at 0.46 and 0.26 V,

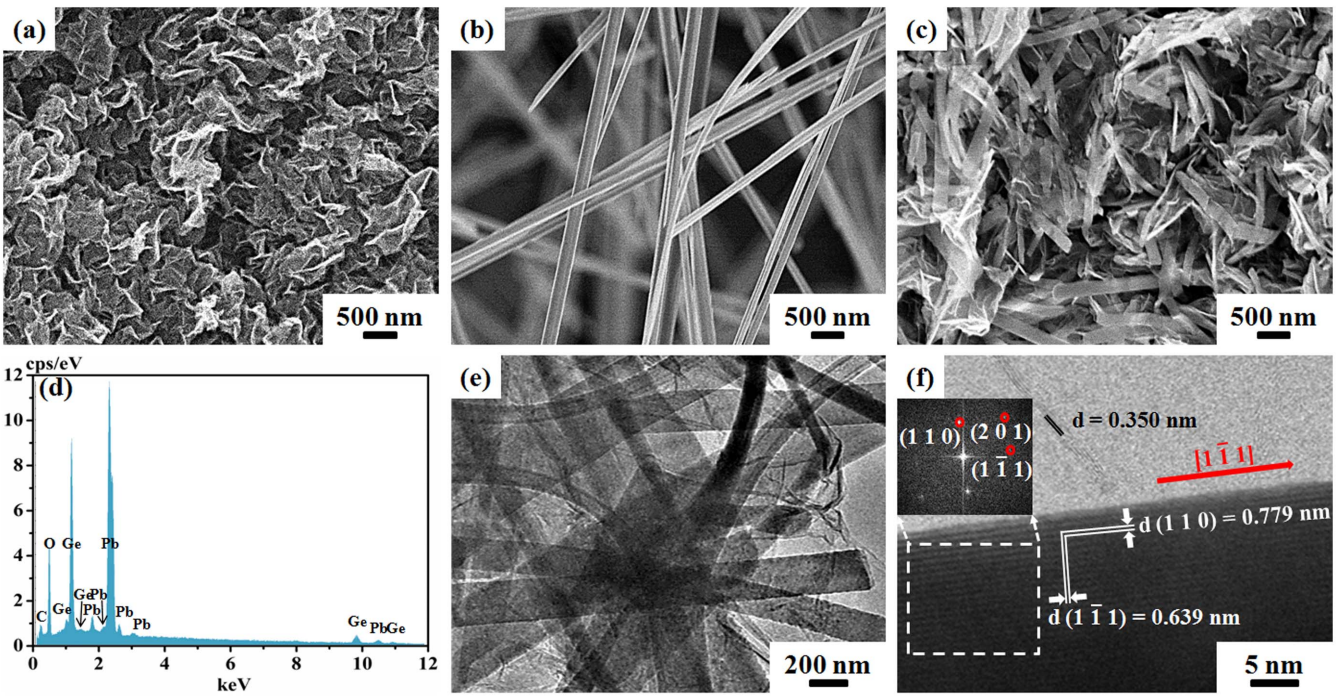

Figure 2 | FE-SEM images of (a) the GNS, (b) the pure $PbGeO_3$, and (c) the $PbGeO_3$-GNS2 (20 wt.%) composite; (d) the corresponding EDS for (c); (e) large area TEM image of the $PbGeO_3$-GNS2 composite; and (f) HRTEM image of the $PbGeO_3$-GNS2 composite taken along a $PbGeO_3$ nanowire wrapped with GNS (inset is the FFT diffractogram of the selected area).

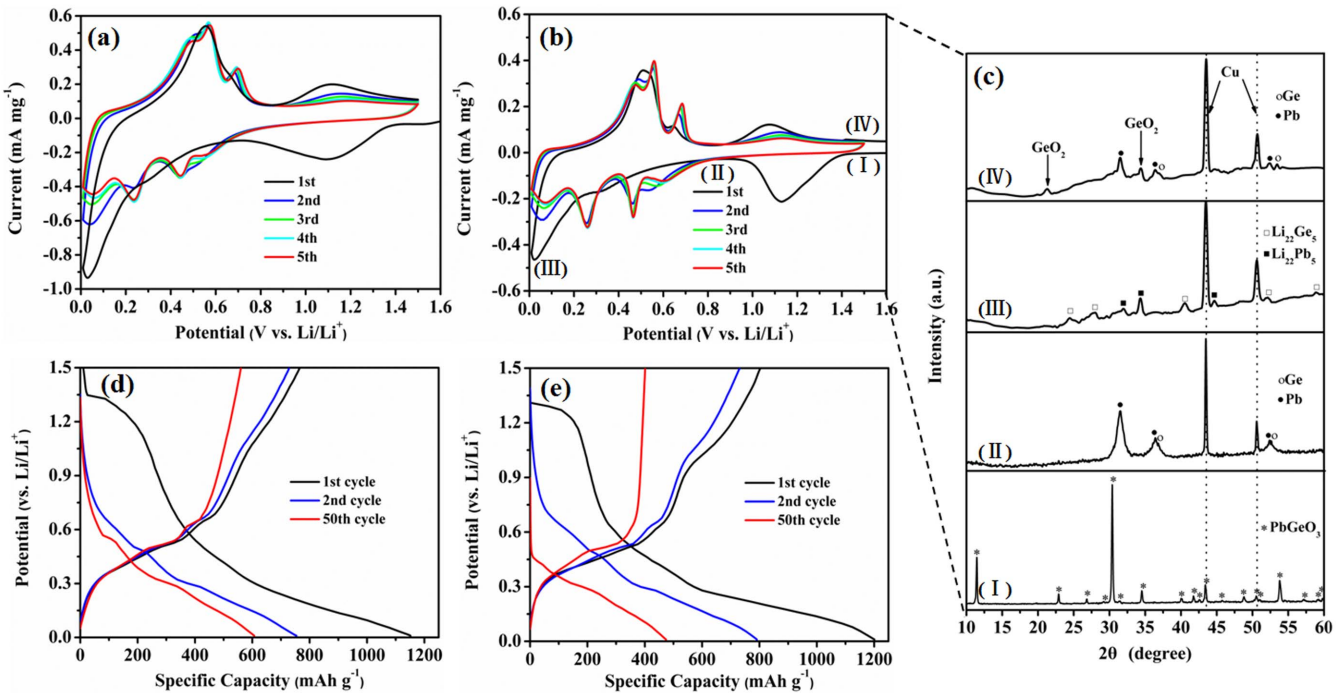

Figure 3 | Cyclic voltammograms for the first 5 cycles of (a) the $PbGeO_3$-GNS2(20 wt.%) anode and (b) the pure $PbGeO_3$ anode; (c) ex-situ XRD patterns of the pure $PbGeO_3$ anode: (I) as-prepared, (II) first discharge to 1.0 V, (III) fully discharged to 0.01 V, and (IV) fully charged to 1.50 V; charge-discharge curves of (d) the $PbGeO_3$-GNS2 anode and (e) the pure $PbGeO_3$ anode for selected cycles.

respectively, followed by their further alloying reactions below 0.2 V[30,32,36]. Pb and Ge diffraction peaks can be detected in the ex-situ XRD patterns after the first discharge to 1.0 V. When the anode is fully discharged to 0.01 V, the diffraction peaks of $Li_{22}Ge_5$ and $Li_{22}Pb_5$ are observed due to the alloying reactions. The peaks are indexed to the formation of Pb, Ge, and GeO_2 at the fully charged stage, and no PbO peak can be found, implying that Pb was not oxidized by Li_2O. These results are well consistent with the CV data discussed above.

Selected galvanostatic charge-discharge profiles of $PbGeO_3$-GNS2(20 wt.%) anode and the pure $PbGeO_3$ anode at the current density of 100 mA g^{-1} from 0.01 to 1.50 V are shown in Fig. 3(d, e). As can be seen from these profiles, the voltage trends of the pure $PbGeO_3$ anode and the $PbGeO_3$-GNS2 anode are in good agreement with their CV curves. The obvious irreversible capacity loss can be traced in both the pure $PbGeO_3$ anode and the $PbGeO_3$-GNS2 anode, which is mainly attributable to the reduction of $PbGeO_3$ to Pb, Ge, and Li_2O, together with the formation of a SEI layer[26]. After 50 cycles, the $PbGeO_3$-GNS2 anode possesses 92% coulombic efficiency (607 mAh g^{-1} discharge capacity and 561 mAh g^{-1} charge capacity), much higher than 85% of those of the pure $PbGeO_3$ anode (474 mAh g^{-1} discharge capacity and 401 mAh g^{-1} charge capacity). Multiple clear plateaus in typical cycles still exist up to 50 cycles, suggesting that the composite anode could maintain good kinetic activity towards lithium ion intercalation/de-intercalation during cycling, which is responsible for the improved coulombic efficiency.

Fig. 4(a) demonstrates the cycling stability of the $PbGeO_3$-GNS composite anodes at the current density of 100 mA g^{-1} from 0.01 to 1.50 V, and the results for pure $PbGeO_3$ anode and for GNS anode are also included for comparison. In the first cycle, the discharge capacity of the pure $PbGeO_3$ is about 1201 mAh g^{-1}, and it gradually drops to 474 mAh g^{-1} after 50 cycles, which is about 39% of the initial capacity. Remarkably, the $PbGeO_3$ nanowires, after being decorated on the GNS, show improved cyclic performance. To be specific, the discharge capacities of the $PbGeO_3$-GNS3(6 wt.%) anode and the $PbGeO_3$-GNS1(36 wt.%) anode are about 538 and 508 mAh g^{-1} after 50 cycles, respectively, still showing 45% and 46% capacity retention. The $PbGeO_3$-GNS2(20 wt.%) anode delivers a reversible capacity of 607 mAh g^{-1}, which is 53% of its initial capacity and 28% higher than that of the pure $PbGeO_3$ anode. The $PbGeO_3$-GNS1 and $PbGeO_3$-GNS3 anodes show lower discharge capacity after 50 cycles due to less $PbGeO_3$ active material and less GN conductive matrix loading, respectively. Therefore, the optimum $PbGeO_3$ content in the composite paper anode is 80 wt.%. Similar synergic effects were also observed in other composite anode systems[37,38].

The current density was also varied to investigate the rate capability of the anodes made from the pure $PbGeO_3$ and $PbGeO_3$-GNS2(20 wt.%) composite in Fig. 4(b). The $PbGeO_3$-GNS2 anode shows larger capacity at each individual current density and 406 mAh g^{-1} at a current density of 1600 mA g^{-1}. After cycling at high current densities, the $PbGeO_3$ and the composite anode were galvanostatically discharged and charged at a current of 100 mA g^{-1} again. Unlike the discharge capacity of the $PbGeO_3$ anode, the discharge capacity of the composite anode recovers to 736 mAh g^{-1}, almost the same as its initial reversible capacity.

The improvements in the electrochemical performance of the $PbGeO_3$-GNS anodes over the pure $PbGeO_3$ anode materials can be ascribed to the uniform encapsulation of the $PbGeO_3$ nanowires in the composite anode in the electrochemically active GNS and the good contact that they maintain with each other. These structural characteristics could enable more efficient lithium diffusion channels for the lithium insertion and de-insertion. Moreover, the GNS could increase the electrical conductivity of the anodes by forming a three-dimensional electrically conductive network. Furthermore, the GNS could provide enough void spaces to limit the Ge particle volume changes and agglomeration, maintaining the structural integrity of the composite anode during the charge–discharge processes.

Electrochemical impedance spectroscopy (EIS) results for the pure $PbGeO_3$ anode and the $PbGeO_3$-GNS2(20 wt.%) anode were collected using a sine wave of 10 mV amplitude over a frequency range of 100 kHz–0.01 Hz, as shown in Fig. 5. To maintain uniformity, the

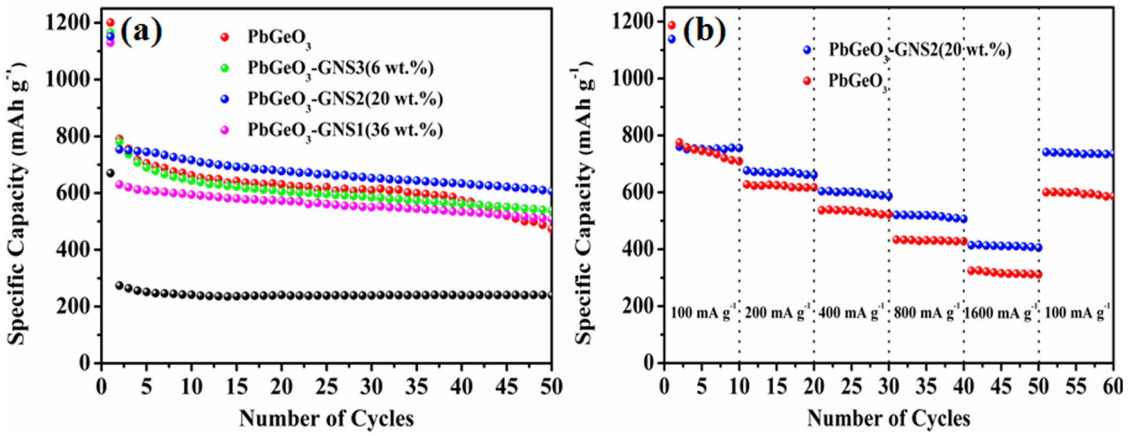

Figure 4 | (a) Cycling stability of the pure $PbGeO_3$ and the $PbGeO_3$-GNS anodes, and (b) rate capability of the pure $PbGeO_3$ and the $PbGeO_3$-GNS2(20 wt.%) anode.

impedance measurements were performed in the fully charged state after running charge-discharge for 50 cycles. The equivalent circuit obtained from the four fitting modes for the Nyquist plots are shown in the inset. All plots exhibit one compressed semicircle in the high frequency region and a sloping line in the low frequency regime. The intercept on the Z_{real} axis in the high frequency region reveals the entire resistance (R_s) of the electrolyte, separator, and electrical contacts. The semicircle in the high frequency range indicates the charge transfer resistance (R_{ct}), which is related to the charge transfer reaction at the electrode/electrolyte interface. The inclined line in the low frequency region represents the Warburg impedance (Z_W), determined by the ion diffusion process in the anode material[39,40].

It should be noted that considerable differences can be observed on comparing the EIS data for the $PbGeO_3$-GNS2(20 wt.%) anode to the data for the pure $PbGeO_3$ anode. On the one hand, the R_{ct} values for the $PbGeO_3$-GNS2 anode before cycling and after 50 cycles are both lower than those of the $PbGeO_3$ anode, respectively. It can be assumed that the GNS in the composite could serve as a highly electrically conductive matrix and enable efficient charge transport at the electrode/electrolyte interface, resulting in suppression of the interparticle resistance of the anode by incorporating the GNS in a composite with $PbGeO_3$. On the other hand, the R_{ct} value after 50 cycles is increased by 130% (from 109 to 251 Ω) for the pure $PbGeO_3$ anode, while there is only an increase of approximately 14% (from 83 to 95 Ω) for $PbGeO_3$-GNS2 anode. Due to the alleviation of Ge volume changes and the particle agglomeration by the GNS in the composite anode during cycling, the electrode integration can be well maintained, which could significantly restrain the increase of R_{ct}.

To characterize the changes in the structure of the $PbGeO_3$-GNS2 composite before and after cycling, a morphological study was conducted on the composite after 50 cycles, and the TEM image is shown in Fig. 6(a). The cycled composite shows a similar morphology to the $PbGeO_3$-GNS2 composite before cycling [see Fig. 2(e)], illustrating that the nanowire structure was retained after 50 cycles. The element distribution in the anode was analysed by EDS over the rectangular region in Figure 6(b). The obtained distributions of different elements are shown in Figure 6(c). The EDS mapping indicates that Pb, Ge, and O are uniformly distributed on the nanowires, and the structural stability of the $PbGeO_3$-GNS2 anode was further confirmed. It was reported previously that germanate nanowire anode could ensure fast Li-ion insertion/removal during cycling, offering excellent electrochemical performance[14,23]. Additionally, the 1-D nanowires are robust enough to maintain the initial morphology, minimizing the strain of the Ge volume change. More importantly, the conductive GNS matrix not only acts as an elastic buffer spacer to further accommodate the Ge volume change, but also prevents the nanowires from agglomerating and restacking during the Li-ion insertion/extraction processes, which is favourable for improving the electrochemical performance of the anode material.

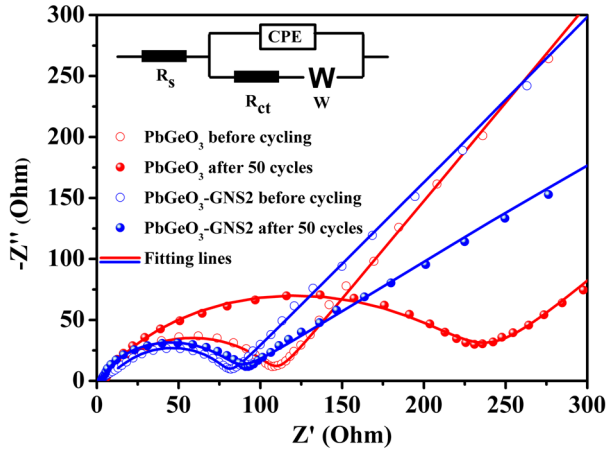

Figure 5 | **Impedance spectra for the pure $PbGeO_3$ anode and the $PbGeO_3$-GNS2(20 wt.%) anode before cycling and after 50 cycles, with the inset showing the equivalent circuit model.**

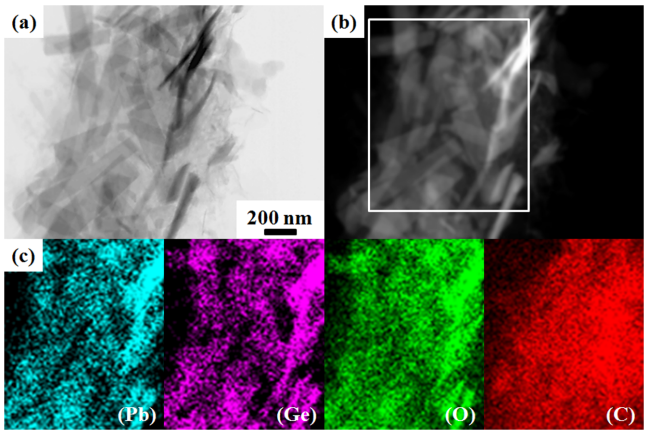

Figure 6 | (a) TEM, (b) STEM, and (c) corresponding element mapping images of the $PbGeO_3$-GNS2(20 wt.%) anode after 50 cycles.

Discussion

In conclusion, novel $PbGeO_3$-GNS composites have been synthesised by a simple and effective in situ hydrothermal method, in which $PbGeO_3$ nanowires with diameters in the range of 100–200 nm are embedded in conductive and interconnected GN networks. The charge-discharge mechanism during cycling is recognized to originate from the decomposition of $PbGeO_3$ into Pb, Ge, and Li_2O, leading to reversible lithiation and de-lithiation for Pb and Ge, accompanied by a partial Ge oxidation reaction by Li_2O. The $PbGeO_3$-GNS anodes exhibit superior cycling performance compared to the pure $PbGeO_3$ anode, delivering enhanced discharge capacities after 50 cycles and displaying obviously improved rate capability. The improvements can be attributed to the GN matrix in the composites, which increases the electrical conductivity of the composite anodes, maintains the structural integrity of the composite anodes by alleviating volume changes and particle agglomeration, and provides more efficient paths for lithium diffusion in the composite anodes, so as to enhance electrochemical activities towards lithium insertion and de-insertion during cycling.

Methods

Synthesis of the $PbGeO_3$-GNS composites. Graphene oxide (GO) was synthesized from natural graphite powder (Fluka) according to a modified Hummers method, as reported elsewhere[41]. To prepare the $PbGeO_3$-GNS composites, 50 mg GO and $Pb(CH_3COO)_2{\cdot}3H_2O$ were first added into 50 mL distilled water and ultrasonically treated for 1 h. The suspension was then mixed with 10 mL GeO_2 solution, followed by constant stirring for 30 min. The mixed solution was then transferred into a 100 mL autoclave with a Teflon liner. The autoclave was maintained at 180°C for 24 h, and then rapidly cooled to room temperature in air. The final products ware collected, washed with deionized water and ethanol three times, and dried in a vacuum oven at 60°C for 12 h. By using this method, three $PbGeO_3$-GNS composites were fabricated using 0.15, 0.3 and 1.5 mmol $Pb(CH_3COO)_2{\cdot}3H_2O$, respectively, and GeO_2 precursor solution with the same amount of GO (50 mg). The composites above are designated as $PbGeO_3$-GNS1, $PbGeO_3$-GNS2, and $PbGeO_3$-GNS3, respectively. The pure GNS and the $PbGeO_3$ were also synthesized by the same method for comparison without the precursor solution and the GO, respectively.

Characterization. X-ray diffraction (XRD, GBC-MMA) patterns were collected on a GBC MMA generator and diffractometer with Cu Kα radiation. Infrared (IR) spectroscopy was conducted using a Shimadazu IRPrestige-21 Fourier transform IR (FT-IR) spectrometer with KBr as the background file. The morphologies of the samples were examined by field emission scanning electron microscopy (FE-SEM, JEOL 7500) and transmission electron microscopy (TEM, JEOL ARM-200F). High-angle annular dark-field (HAADF) scanning transmission electron microscope (STEM) images and corresponding element mapping images were collected with the same TEM equipped with a Centurio SSD energy-dispersive X-ray spectroscopy (EDS) detector. Thermogravimetric analysis (TGA) was performed using a SETARAM Thermogravimetric Analyzer (France).

Electrochemical measurements. CR 2032 coin-type cells with the working electrode containing 80 wt.% active materal, 10 wt.% carbon black, and 10 wt.% carboxymethyl cellulose (CMC) on copper foil were assembled in an Ar-filled glove box (Mbraun, Unilab, Germany), using lithium metal foil as the counter electrode. The electrolyte used in assembling the cells and washing the electrodes for ex-situ XRD was $LiPF_6$ (1 M) in a 50 : 50 (v/v) mixture of ethylene carbonate (EC) and diethyl carbonate (DEC). Cyclic voltammetry (CV) was conducted on an electrochemistry workstation (Biologic VMP-3). The specific capacities were calculated based on the amount of active material in the electrode. Electrochemical impedance spectroscopy (EIS) was carried out utilizing a CHI 660B electrochemical workstation.

1. Armand, M. & Tarascon, J. M. Building better batteries. *Nature* **451**, 652–657 (2008).
2. Bruce, P. G., Scrosati, B. & Tarascon, J. M. Nanomaterials for rechargeable lithium batteries. *Angewandte Chemie* **47**, 2930–2946 (2008).
3. Li, H., Wang, Z., Chen, L. & Huang, X. Research on Advanced Materials for Li-ion Batteries. *Advanced Materials* **21**, 4593–4607 (2009).
4. Wang, J. *et al.* A germanium/single-walled carbon nanotube composite paper as a free-standing anode for lithium-ion batteries. *J. Mater. Chem. A* **2**, 4613–4618 (2014).
5. Li, W. H. *et al.* Germanium nanoparticles encapsulated in flexible carbon nanofibers as self-supported electrodes for high performance lithium-ion batteries. *Nanoscale* **6**, 4532–4537 (2014).
6. Tan, L. P. *et al.* Germanium nanowires-based carbon composite as anodes for lithium-ion batteries. *J. Power Sources* **206**, 253–258 (2012).
7. Zhong, C., Wang, J. Z., Gao, X. W., Wexler, D. & Liu, H. K. In situ one-step synthesis of a 3D nanostructured germanium-graphene composite and its application in lithium-ion batteries. *J. Mater. Chem. A* **1**, 10798–10804 (2013).
8. Chan, C. K., Zhang, X. F. & Cui, Y. High capacity Li ion battery anodes using Ge nanowires. *Nano Lett.* **8**, 307–309 (2008).
9. Hwang, I. S. *et al.* A binder-free Ge-nanoparticle anode assembled on multiwalled carbon nanotube networks for Li-ion batteries. *Chemical communications* **48**, 7061–7063 (2012).
10. Yang, L. C., Gao, Q. S., Li, L., Tang, Y. & Wu, Y. P. Mesoporous germanium as anode material of high capacity and good cycling prepared by a mechanochemical reaction. *Electrochemistry Communications* **12**, 418–421 (2010).
11. Lee, H. *et al.* Surface-stabilized amorphous germanium nanoparticles for lithium-storage material. *J. Phys. Chem. B* **109**, 20719–20723 (2005).
12. Kim, C. H., Jung, Y. S., Lee, K. T., Ku, J. H. & Oh, S. M. The role of in situ generated nano-sized metal particles on the coulombic efficiency of $MGeO_3$ (M = Cu, Fe, and Co) electrodes. *Electrochim. Acta* **54**, 4371–4377 (2009).
13. Feng, J. K., Lai, M. O. & Lu, L. Zn_2GeO_4 Nanorods synthesized by low-temperature hydrothermal growth for high-capacity anode of lithium battery. *Electrochemistry Communications* **13**, 287–289 (2011).
14. Li, W. W. *et al.* Highly Reversible Lithium Storage in Hierarchical $Ca_2Ge_7O_{16}$ Nanowire Arrays/Carbon Textile Anodes. *Chem.-Eur. J.* **19**, 8650–8656 (2013).
15. Pan, Q. M., Wang, Z. J., Liu, J., Yin, G. P. & Gu, M. PbO@C core-shell nanocomposites as an anode material of lithium-ion batteries. *Electrochem. Commun.* **11**, 917–920 (2009).
16. Shu, J. *et al.* Hydrothermal fabrication of lead hydroxide chloride as a novel anode material for lithium-ion batteries. *Electrochim. Acta* **102**, 381–387 (2013).
17. Feng, J. *et al.* Low temperature synthesis of lead germanate ($PbGeO_3$)/polypyrrole (PPy) nanocomposites and their lithium storage performance. *Materials Research Bulletin* **57**, 238–242 (2014).
18. Kim, H., Park, K. Y., Hong, J. & Kang, K. All-graphene-battery: bridging the gap between supercapacitors and lithium ion batteries. *Sci. Rep.* **4**, 5278–5286 (2014).
19. Zhong, C., Wang, J.-Z., Wexler, D. & Liu, H.-K. Microwave autoclave synthesized multi-layer graphene/single-walled carbon nanotube composites for free-standing lithium-ion battery anodes. *Carbon* **66**, 637–645 (2014).
20. Zhu, J. *et al.* Graphene double protection strategy to improve the SnO_2 electrode performance anodes for lithium-ion batteries. *Nano Energy* **3**, 80–87 (2014).
21. Zhang, B. H. *et al.* Nanowire $Na_{0.35}MnO_2$ from a hydrothermal method as a cathode material for aqueous asymmetric supercapacitors. *Journal of Power Sources* **253**, 98–103 (2014).
22. Zhang, B. H. *et al.* Nanowire $K_{0.19}MnO_2$ from hydrothermal method as cathode material for aqueous supercapacitors of high energy density. *Electrochimica Acta* **130**, 693–698 (2014).
23. Chen, Z. *et al.* Copper germanate nanowire/reduced graphene oxide anode materials for high energy lithium-ion batteries. *J. Mater. Chem. A* **1**, 11404–11409 (2013).
24. Wang, Y. X. *et al.* Ultrafine SnO_2 nanoparticle loading onto reduced graphene oxide as anodes for sodium-ion batteries with superior rate and cycling performances. *Journal of Materials Chemistry A* **2**, 529–534 (2014).
25. Guo, H. L., Wang, X. F., Qian, Q. Y., Wang, F. B. & Xia, X. H. A Green Approach to the Synthesis of Graphene Nanosheets. *ACS Nano* **3**, 2653–2659 (2009).
26. Shi, Y. *et al.* In-situ hydrothermal synthesis of graphene woven VO_2 nanoribbons with improved cycling performance. *Journal of Power Sources* **244**, 684–689 (2013).
27. Zhou, J., Song, H., Ma, L. & Chen, X. Magnetite/graphene nanosheet composites: interfacial interaction and its impact on the durable high-rate performance in lithium-ion batteries. *RSC Advances* **1**, 782–791 (2011).
28. Karthikeyan, K., Kalpana, D., Amaresh, S. & Lee, Y. S. Microwave synthesis of graphene/magnetite composite electrode material for symmetric supercapacitor with superior rate performance. *RSC Advances* **2**, 12322–12328 (2012).
29. Shi, Y. *et al.* Hollow structured Li_3VO_4 wrapped with graphene nanosheets in situ prepared by a one-pot template-free method as an anode for lithium-ion batteries. *Nano letters* **13**, 4715–4720 (2013).
30. Seng, K. H., Park, M. H., Guo, Z. P., Liu, H. K. & Cho, J. Self-assembled germanium/carbon nanostructures as high-power anode material for the lithium-ion battery. *Angewandte Chemie* **51**, 5657–5661 (2012).
31. Ng, S. H. *et al.* Spray Pyrolyzed PbO-Carbon Nanocomposites as Anode for Lithium-Ion Batteries. *Journal of The Electrochemical Society* **153**, A787–A793 (2006).
32. Seng, K. H., Park, M. H., Guo, Z. P., Liu, H. K. & Cho, J. Catalytic role of Ge in highly reversible GeO_2/Ge/C nanocomposite anode material for lithium batteries. *Nano letters* **13**, 1230–1236 (2013).
33. Li, W. *et al.* Single-crystalline metal germanate nanowire-carbon textiles as binder-free, self-supported anodes for high-performance lithium storage. *Nanoscale* **5**, 10291–10299 (2013).
34. Yuan, Z., Peng, Z., Chen, Y. & Liu, H. Synthesis and electrochemical performance of nanosized tin lead composite oxides as lithium storage materials. *Materials Chemistry and Physics* **120**, 331–335 (2010).
35. Tovar, L. L. G., Connor, P. A., Belliard, F., Torres-Martinez, L. M. & Irvine, J. T. S. Investigation of lead tin fluorides as possible negative electrodes for Li-ion batteries. *J. Power Sources* **97–8**, 258–261 (2001).
36. Martos, M., Morales, J. & Sanchez, L. Lead-based systems as suitable anode materials for Li-ion batteries. *Electrochim. Acta* **48**, 615–621 (2003).

37. Gao, X. W., Wang, J. Z., Chou, S. L. & Liu, H. K. Synthesis and electrochemical performance of LiV_3O_8/polyaniline as cathode material for the lithium battery. *Journal of Power Sources* **220**, 47–53 (2012).
38. Chou, S. L. *et al.* High-surface-area α-Fe2O3/carbon nanocomposite: one-step synthesis and its highly reversible and enhanced high-rate lithium storage properties. *Journal of Materials Chemistry* **20**, 2092–2098 (2010).
39. Gao, X. W. *et al.* $LiNi_{0.5}Mn_{1.5}O_4$ spinel cathode using room temperature ionic liquid as electrolyte. *Electrochimica Acta* **101**, 151–157 (2013).
40. Zhang, Z. J. *et al.* Tuning three-dimensional TiO_2 nanotube electrode to achieve high utilization of Ti substrate for lithium storage. *Electrochimica Acta* **133**, 570–577 (2014).
41. Cote, L. J., Kim, F. & Huang, J. X. Langmuir-Blodgett Assembly of Graphite Oxide Single Layers. *J. Am. Chem. Soc.* **131**, 1043–1049 (2009).

Acknowledgments

Jun Wang is grateful to the China Scholarship Council (CSC) for scholarship support. The authors acknowledge the use of facilities funded by the Australian Research Council (ARC)-LIEF Grant LE120100104 in the UOW Electron Microscopy Centre. Many thanks are also owed to Dr. Tania Silver for critical reading of the manuscript.

Author contributions

J.Z.W. and C.Q.F. designed the work; J.W. performed the experiments. Z.Q.S. helped to conduct the TEM measurements. J.W. wrote the manuscript. J.Z.W., S.L.C. and H.K.L. contributed to discussions and reviewing the manuscript.

Additional information

Competing financial interests: The authors declare no competing financial interests.

How to cite this article: Wang, J. *et al. In-situ* One-step Hydrothermal Synthesis of a Lead Germanate-Graphene Composite as a Novel Anode Material for Lithium-Ion Batteries. *Sci. Rep.* **4**, 7030; DOI:10.1038/srep07030 (2014).